PAPER

Check for updates

Terthiophene based low-cost fully non-fused electron acceptors for high-efficiency as-cast organic solar cells†

Yuanyuan Zhou,[ab] Peng Liu,[a] Shuaishuai Shen,[c] Miao Li,*[ab] Ruiping Qin, [iD] [a] XiaoDan Tang,[a] ChaoChao Qin,[e] Jinsheng Song, [iD] *[b] Zhishan Bo [iD] *[d] and Lei Zhang [iD] *[c]

Fully non-fused electron acceptors (FNEAs) have shown a promising prospect for commercial applications of organic solar cells (OSCs) due to their simple structures and low costs. Herein, two terthiophene-based NFEAs **3T-1** and **3T-2** were exploited from a single thiophene ring as the starting material. Octyl substituted **3T-1** exhibits strong crystallinity, poor miscibility, and forms large aggregates when blending with polymer **D18**, leading to an inferior power conversion efficiency (PCE). While 2-ethylhexyl substituted **3T-2** possesses good solubility and enhanced compatibility with polymer **D18**, the blend film exhibits an appropriate morphology, face-on molecular orientation, and efficient charge transport. As a result, the as-cast device based on **3T-2** exhibits a significantly enhanced PCE of 11.12% processed by non-halogenated *o*-xylene as the solvent, which is the highest value of terthiophene based FNEAs for OSCs so far. Our work provides insight into molecular design of FNEAs for high-performance OSCs.

Introduction

Organic solar cells (OSCs) as a potentially sustainable energy technology have drawn considerable attention owing to their flexibility, light weight and solution-processability in comparison with their inorganic counterparts.[1–4] Benefiting from the development of fused ring electron acceptors (FREAs), the power conversion efficiencies (PCEs) of OSCs have been significantly improved.[5–9] Highly efficient FREAs generally have an acceptor–donor–acceptor (A–D–A) type molecular structure with a multi-fused ring core as the D unit and two cyanoindanone type terminal groups as the A unit.[10–13] The π-extended fused ring cores play a critical role in achieving excellent photovoltaic performance. The conjugated fused ring building blocks usually possess planar and rigid configurations, which are beneficial for π-electron delocalization and intramolecular charge transport. In the

meantime, the bulky side chains on the fused-ring building blocks can regulate molecular solubility and crystallinity, and provide suitable phase separation morphology to the blend film. In 2019, Zou *et al.* exploited a novel FREA Y6 with a N-hetero-fused-ring building block as the core.[11] To date, the PCEs based on Y-series FREAs have exceeded 19% for single bulk-heterojunction OSCs.[14–16] Nevertheless, these multi-fused ring cores of FREAs generally require tedious syntheses, which inevitably give rise to the low yields and expensive preparation costs. Therefore, the development of high efficiency and low-cost acceptor materials with simple molecular structures is an essential step to achieve the large-scale commercial applications for OSCs.[17–21]

Up to now, great efforts have been devoted to exploiting fully non-fused electron acceptors (FNEAs), which commonly consist of two or more benzene and thiophene rings linked by a C–C single bond as D units instead of a complex multi-fused ring core.[22–27] On the other hand, introduction of intramolecular noncovalent interactions is an efficient method to form ladder-like structures, which can effectively prevent the low-yield ring-closure step and reduce synthetic costs. Oligothiophenes have been widely used as organic semiconductors in organic field-effect transistors and OSCs due to their good hole transport abilities and tunable optical/electrochemical properties together with their relatively simple synthesis, and high stability.[28–32] Very recently, oligothiophenes as fully non-fused cores have been employed to construct high efficiency FNEAs. After comprehensive analysis of the current reports on oligothiophene cores, there are mainly two reported ways to conduct structural modifications: (i) changing the number of thiophene rings can control the length of the

aSchool of Materials Science and Engineering, Henan Key Laboratory of Photovoltaic Materials, Henan Normal University, Xinxiang, 453007, China. E-mail: limiao2020@htu.edu.cn

bEngineering Research Center for Nanomaterials, Henan University, Kaifeng, 475004, China. E-mail: songjs@henu.edu.cn

cBeijing University of Chemical Technology, Beijing, 100875, China. E-mail: zhl@mail.buct.edu.cn

dBeijing Key Laboratory of Energy Conversion and Storage Materials, College of Chemistry, Beijing Normal University, Beijing, 100875, China. E-mail: zsbo@bnu.edu.cn

eSchool of Physics, Henan Normal University, Xinxiang, 453007, China

† Electronic supplementary information (ESI) available. See DOI: https://doi.org/10.1039/d3ta00372h

conjugate skeleton; such as bithiophene,[33] terthiophene,[24,34] and tetrathiophene;[35,36] (ii) the functional side chain groups of the thiophene ring can induce the formation of noncovalent intramolecular interactions, and tune molecular solubility, packing and crystallinity.[37,38] For example, Hou *et al.* reported a tetrathiophene based FNEA A4T-16 with bulky functional group 2,4,6-triisopropylphenyl as the side chain. A4T-16 can form a three-dimensional interpenetrating network and compact π–π stacking, leading to a record PCE of 15.2%.[39] Subsequently, our group synthesized a tetrathiophene based FNEA 4T-3 with branched 2-ethylhexyl chains and a PCE of 12.04%, and a high figure-of-merit (FOM) value of 32.8 can be achieved.[35] Compared to tetrathiophene-based FNEAs, terthiophene-based acceptors have simpler molecular structures. However, there have been limited reports on terthiophene-based FNEAs with a PCE of about 7%.[24,34] Hence, designing terthiophene based FNEAs is still a challenge to realize effective photovoltaic performance for OSCs.

Herein, we report two terthiophene based FNEAs **3T-1** and **3T-2** with octyl and 2-ethylhexyl side chains, respectively. The two FNEAs are readily prepared from commercially available thiophene derivatives in high yields. Our results demonstrated that side chain engineering could regulate the molecular miscibility and crystallinity, which in turn control the morphology and molecular orientation in thin films. **3T-1** displays strong crystallinity and poor miscibility with the polymer donor **D18**, resulting in an apparent phase separation with an edge-on molecular orientation in the blend film. In comparison, **3T-2** has good miscibility with **D18**; the blend film exhibits a homogenous morphology, face-on molecular orientation and high and balanced charge mobility. As a result, the as-cast devices based on **3T-2** can achieve an excellent PCE of 11.12% processed by non-halogenated *o*-xylene as the solvent, which is the highest value for terthiophene based FNEAs for OSCs.

Results and discussion

Synthesis

Scheme 1 shows the synthesis of **3T-1** and **3T-2**. The starting materials (**1** and **2**) were prepared according to previously reported procedures.[40,41] A Stille coupling of 2,5-dibromo-3,4-alkylthiophene (**1**) and compound **2** afforded **3a** and **3b**, respectively. Subsequently, the dialdehydes (**4a** and **4b**) were prepared *via* the Vilsmeier–Haack reaction. Finally, two terthiophene based acceptors **3T-1** and **3T-2** are obtained in 87% and 91% yields by Knoevenagel condensation with dialdehyde

intermediates and 3-(1,1-dicyanomethylene)-5,6-difluoro-1-indanone (2F-IC). The structures of **3T-1** and **3T-2** were confirmed by ^{1}H and ^{13}C NMR spectroscopy and mass spectrometry. **3T-2** are highly soluble in common halogenated solvents such as dichloromethane, chloroform, *o*-dichlorobenzene and non-halogenated solvents such as *o*-xylene at room temperature; however, **3T-1** are less soluble in the abovementioned solvents.

Optical and electrochemical properties

The chemical structures of the two terthiophene based FNEAs (**3T-1** and **3T-2**) and the wide bandgap polymer donor **D18** are shown in Fig. 1a.[42] The ultraviolet-visible (UV-vis) absorptions of **3T-1** and **3T-2** characterized in dilute chloroform solutions and as thin films are presented in Fig. 1 and Table 1. The main difference between **3T-1** and **3T-2** is the lateral chains on the molecular skeleton, which has a significant impact on molecular crystallization and the molecular packing in the solid state. Two acceptors **3T-1** and **3T-2** have broad and featureless absorption in solutions with the maximum absorption peaks located at 660 and 642 nm, respectively. Besides, their corresponding molar absorption coefficients are 1.87×10^5 and 1.85×10^5 M^{-1} cm^{-1} (Fig. S1†), respectively. From solutions to thin films, the absorptions of **3T-1** and **3T-2** change significantly, and both exhibit 0–0 and 0–1 absorption peaks. Compared to the absorption spectra in solutions, the absorption in the solid films covers the 500 to 850 nm region, and the main absorption peak is located at 762 and 740 nm for **3T-1** and **3T-2**, respectively. The large red-shift (~100 nm) is probably due to the formation of *J*-aggregation in the solid state. Meanwhile, **3T-1** possesses a more red-shifted and intensified 0–0 peak than **3T-2**, which indicates a stronger intermolecular interaction and more ordered molecular packing for **3T-1**. Two acceptor molecules and the polymer donor **D18** display complementary absorption spectra with coverage from 300 nm to 850 nm, which offers a prerequisite for better utilization of solar radiation. According to the equation $E_g^{opt} = 1240/\lambda_{onset}$, the optical bandgaps of **3T-1** and **3T-2** can be estimated to be 1.47 and 1.48 eV, respectively. In addition, the energy levels of **3T-1** and **3T-2** are evaluated by the electrochemical method. The cyclic voltammetry curves are exhibited in Fig. S2† and the details are shown in Fig. 1d and Table 1. According to the equation $E_{HOMO/LUMO} = -e(E_{onset,ox/red} - E_{Fc/Fc+} + 4.80)$, their highest occupied molecular orbital (HOMO) can be determined to be −5.77 and −5.92 eV, and the lowest unoccupied molecular orbital (LUMO) energy levels are −3.54 and
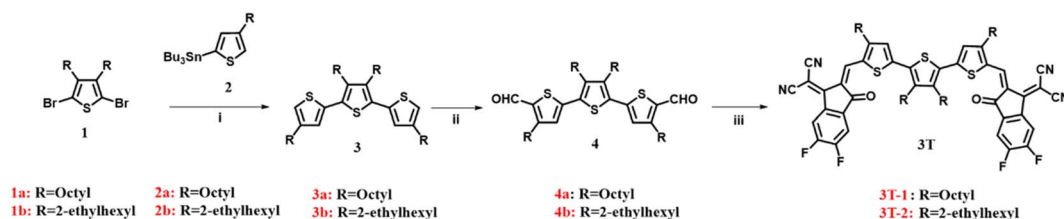
Scheme 1 The synthetic routes of **3T-1** and **3T-2**. Conditions and reagents: (i) Pd(PPh$_3$)$_4$, toluene, 110 °C; (ii) POCl$_3$, DMF, 1,2-dichloroethane, 85 °C; (iii) 3-(1,1-dicyanomethylene)-5,6-difluoro-1-indanone, CHCl$_3$, pyridine, 25 °C.

1a: R=Octyl   **2a:** R=Octyl   **3a:** R=Octyl   **4a:** R=Octyl   **3T-1:** R=Octyl
1b: R=2-ethylhexyl   **2b:** R=2-ethylhexyl   **3b:** R=2-ethylhexyl   **4b:** R=2-ethylhexyl   **3T-2:** R=2-ethylhexyl

This journal is © The Royal Society of Chemistry 2023

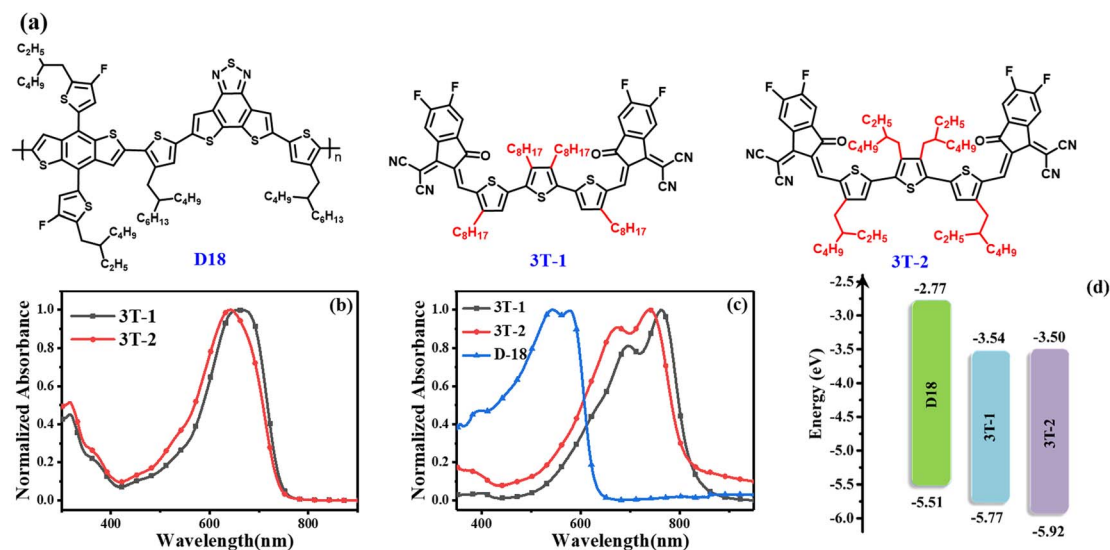*J. Mater. Chem. A*, 2023, **11**, 7498–7504 | **7499**

Fig. 1 (a) Molecular structures of D18, 3T-1 and 3T-2; (b) the normalized absorption spectra of 3T-1 and 3T-2 in chloroform solutions; (c) the normalized absorption spectra of the thin films for D18, 3T-1 and 3T-2; (d) energy level diagrams of the three materials D18, 3T-1 and 3T-2.

Table 1 Optical and electrochemical properties of 3T-1 and 3T-2

| Compound | Solution | | Film | | HOMO (eV) | LUMO (eV) | E_g^{opt} (eV) |
	λ_{max} (nm)	λ_{onset} (nm)	λ_{max} (nm)	λ_{onset} (nm)			
3T-1	660	748	762	843	−5.77	−3.54	1.47
3T-2	642	751	740	836	−5.92	−3.50	1.48

−3.50 eV, respectively. 3T-2 shows a slightly high-lying LUMO level, which may be beneficial to obtain a high V_{oc} for the OSCs.

Quantum calculations

Density functional theory (DFT) calculations at the B3LYP/6-31G (d,p) level are carried out to evaluate the optimal molecular geometries of 3T-1 and 3T-2. To simplify the calculations, the octyl and 2-ethylhexyl side chains are simplified to methyl and 1-methylethyl groups, respectively. As shown in Fig. S3,† the side chains of the thiophene ring would produce different influences in the dihedral angle between the center core and two cyanoindanone type terminal groups. For 3T-1, two small dihedral angles are 0.25° and 0.19°. For 3T-2, the dihedral angles are 5.73° and 0.79°, respectively. The more twisted molecular conformation of 3T-2 may be conducive to reduce the molecular crystallinity and suppress the oversized aggregation in the film.

Photovoltaic properties

To investigated the photovoltaic properties of 3T-1 and 3T-2, OSCs were fabricated with a typical conventional device structure of ITO/PEDOT:PSS/active layer/PDINN/Ag. Here, a wide-bandgap polymer of D18 was selected as the donor polymer and aliphatic amine-functionalized perylene-diimide (PDINN) was chosen as the cathode interlayer. The device evaluation

processes were systematically optimized, including the donor/acceptor ratio, additive concentration and thermal annealing temperature. The optimal photovoltaic performance can be achieved by using non-halogenated o-xylene as the processing solvent and the optimal donor/acceptor ratio of 1 : 1, without an additive and thermal annealing. The current density–voltage (J–V) curves of the optimized devices are depicted in Fig. 2, and the details are listed in Table 2. Although two terthiophene based acceptors possess the same molecular skeleton, an inferior PCE of 2.43% is obtained with a low J_{sc} of 7.11 mA cm^{-2}, an FF of 40.80%, and a V_{oc} of 0.84 V for the as-cast 3T-1-based device. When side chains were changed from the linear octyl chains to branched 2-ethylhexyl chains, the as-cast OSCs based on 3T-2 can achieve a higher V_{oc} of 0.87 V due to the higher LUMO energy level of 3T-2 than that of 3T-1. Meanwhile an obviously enhanced J_{sc} of 17.85 mA cm^{-2} and an increased FF of 71.21% were achieved for the 3T-2-based device, contributing to a significantly enhanced PCE of 11.12%, which is among the highest values of terthiophene based fully non-fused electron acceptors. The enhancements in both the J_{sc} and FF values are mainly ascribed to the improved charge transport and film morphology. The external quantum efficiency (EQE) spectra of 3T-1 and 3T-2 based devices are shown in Fig. 2b. The two devices both exhibit a photoelectric response in the range of 300 nm to 850 nm and the one based on 3T-2 even possesses a maximum value of 75%, indicating that an efficient photon
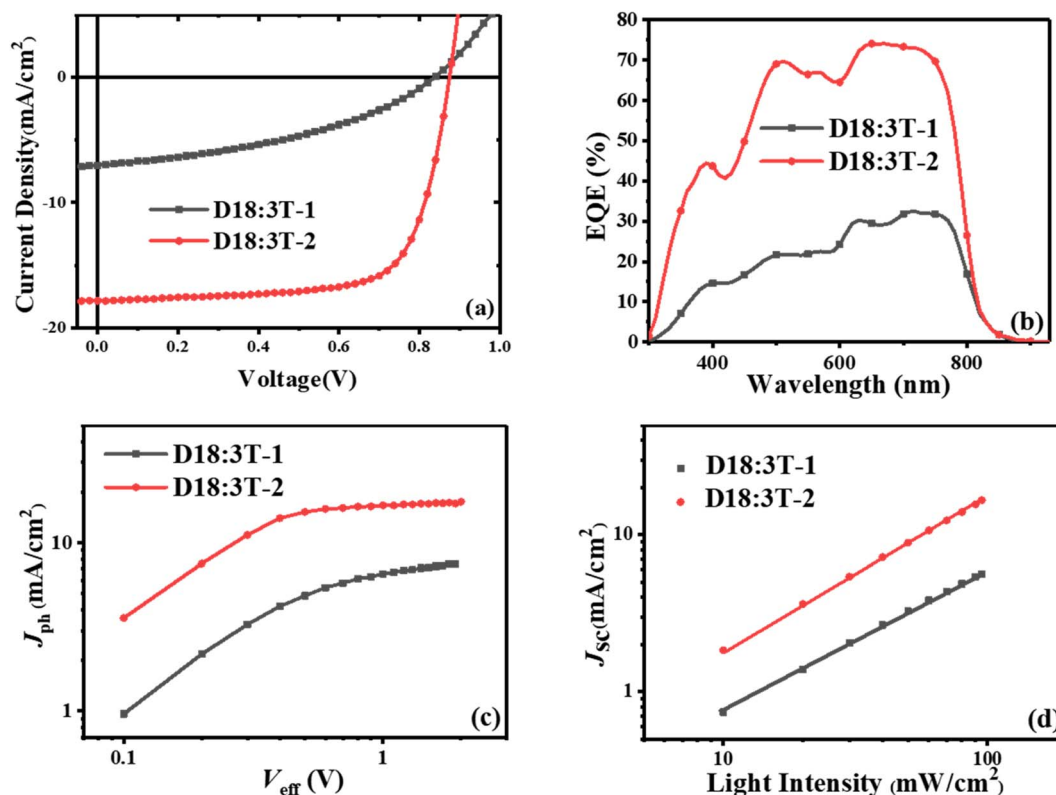
7500 | J. Mater. Chem. A, 2023, 11, 7498–7504

This journal is © The Royal Society of Chemistry 2023

Fig. 2 (a) J–V curves and (b) EQE curves, (c) photocurrent *versus* effective voltage (J_{ph}–V_{eff}) characteristics and (d) light intensity dependence of the optimized **3T-1** and **3T-2** based devices.

Table 2 Photovoltaic performance of the optimized **3T-1** and **3T-2** based devices

Active layer	V_{oc} (V)	J_{sc} (mA cm^{-2})	FF (%)	PCE (%)
D18:3T-1	0.84 (0.832 ± 0.007)	7.11 (6.78 ± 0.17)	40.80 (41.07 ± 1.36)	2.43 (2.32 ± 0.09)
D18:3T-2	0.87 (0.873 ± 0.005)	17.85 (17.73 ± 0.23)	71.21 (69.94 ± 1.04)	11.12 (10.85 ± 0.25)

harvesting and conversion process takes place in the as-cast thin films. Moreover, the current density integrated by EQE curves was 6.92 and 17.58 mA cm^{-2} for **3T-1** and **3T-2** based devices, which are all within 5% deviation from the J–V curves.

To further investigate the exciton dissociation and charge collection in the **3T-1** and **3T-2**-based devices, the photocurrent density (J_{ph}) *versus* effective voltage (V_{eff}) was measured, and the results are shown in Fig. 2c. Under the short-circuit conditions, the abilities of exciton dissociation and charge recombination can be evaluated from the normalized photocurrent density ($P_{diss} = J_{ph}/J_{sat}$, where J_{sat} refers to the saturation photocurrent density). The **3T-1**-based device could not achieve an effective J_{sat}, which indicates that charge recombination occurred in the active layer. In comparison, the P_{diss} can be calculated to be 98.3% for the **3T-2**-based as-cast device, indicating effective exciton dissociation, charge transport and collection in the active layer. Meanwhile, the charge recombination of **3T-1** and **3T-2**-based devices was studied by measuring the current densities under various light intensities (P_{light}). The J_{sc} dependence on P_{light} can be expressed as $J_{sc} \propto P_{light}^{\alpha}$, where the

exponent α value reflects the bimolecular recombination information. As shown in Fig. 2d, the α values of **3T-1** and **3T-2**-based devices are estimated to be 0.89 and 0.98, respectively. The α value of the device based on **3T-2** is close to unity, indicating that the bimolecular recombination can be effectively suppressed in the active layer, which is beneficial for obtaining a high FF for OSCs.

Charge transport mobilities

In order to study the influence of side chains on charge transport properties, space-charge-limited-current (SCLC) measurements were carried out to measure the hole and electron mobilities. The structures of hole-only and electron-only based devices are ITO/PEDOT:PSS/active layer/Au and ITO/ZnO/active layer/PDINN/Ag, respectively. The detailed results are summarized in Table 3 and Fig. S4.† The **D18:3T-1** blend film shows inferior hole mobilities (μ_h) and electron mobilities (μ_e) of 5.77 × 10^{-5} and 1.29 × 10^{-5} cm^2 V^{-1} s^{-1}, respectively. In comparison, the **D18:3T-2** blend film can achieve a high μ_h and μ_e of 1.99 × 10^{-4} and 1.49 × 10^{-4} cm^2 V^{-1} s^{-1}. And the

This journal is © The Royal Society of Chemistry 2023

J. Mater. Chem. A, 2023, **11**, 7498–7504 | **7501**

Table 3 Charge transport mobilities of **3T-1** and **3T-2** based blend films

Active layer	μ_h [cm^2 V^{-1} s^{-1}]	μ_e [cm^2 V^{-1} s^{-1}]	μ_h/μ_e
D18:3T-1	5.77×10^{-5}	1.29×10^{-5}	4.47
D18:3T-2	1.99×10^{-4}	1.49×10^{-4}	1.34

corresponding μ_h/μ_e ratio is calculated to be 4.47 and 1.34 for **3T-1** and **3T-2** based blends, respectively. The excellent μ_e nearly ten times higher than that of the **3T-1**-based blend and more balanced charge transport account for the higher J_{sc} and FF in the **3T-2**-based devices, and thus, a better device performance.

Film morphology

Atomic force microscope (AFM) measurements were utilized to explore the crystallinity properties and aggregation behaviors for **3T-1** and **3T-2** (Fig. 3). Due to the strong crystallinity of **3T-1**, the neat film exhibits quite rough a surface with an extremely large root-mean-square (RMS) value of 12.6 nm, while a smooth surface can be observed in the pure **3T-2** film with a very small RMS value of 0.38 nm. When blending with polymer **D18**, the **D18:3T-1** blend film shows some bright-dark areas with a large RMS value of 13.4 nm, indicating large size phase separation,

which is due to the poor compatibility and strong crystallinity of **3T-1**. In comparison, the **D18:3T-2** blend film displays a uniform surface morphology without large size aggregates formed, which can facilitate exciton dissociation and charge transfer.

To gain insight into the impacts of side chains on the molecular orientation and crystalline properties in the pure and blend films, the grazing-incidence wide-angle X-ray scattering (GIWAXS) measurements were performed. As shown in Fig. 4, for the neat **3T-1** film, distinguishable (010) π–π stacking diffraction peaks at $q = 1.72$ Å^{-1} ($d = 3.65$ Å) in the in-plane (IP) direction can be observed, indicating the edge-on orientations. The pronounced lamellar stacking peaks (100) and (200) at $q = 0.37$ Å^{-1} and $q = 0.74$ Å^{-1} in the out-of-plane (OOP) direction suggest the highly ordered structure of **3T-1**, with the corresponding lamellar stacking distances of 16.97 Å. For the neat **3T-2** film, an extremely weak (010) π–π stacking diffraction peak in the OOP direction and a (100) lamellar diffraction peak in the IP direction can be observed, indicating a face-on molecular orientation. In addition, the crystal coherence length (CCL) values of the (100) diffraction are 161.4 and 41.7 Å for the neat **3T-1** and **3T-2** films, respectively. After blending with polymer donor **D18**, the independent GIWAXS scattering signals originating from **3T-1** are still maintained in the **D18:3T-1** blend
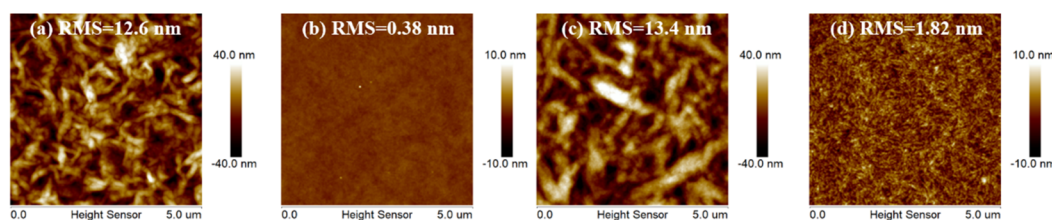

Fig. 3 AFM images of the pure and blend films: (a) the neat **3T-1** film, (b) the neat **3T-2** film, (c) the **D18:3T-1** blend film, and (d) the **D18:3T-2** blend film.
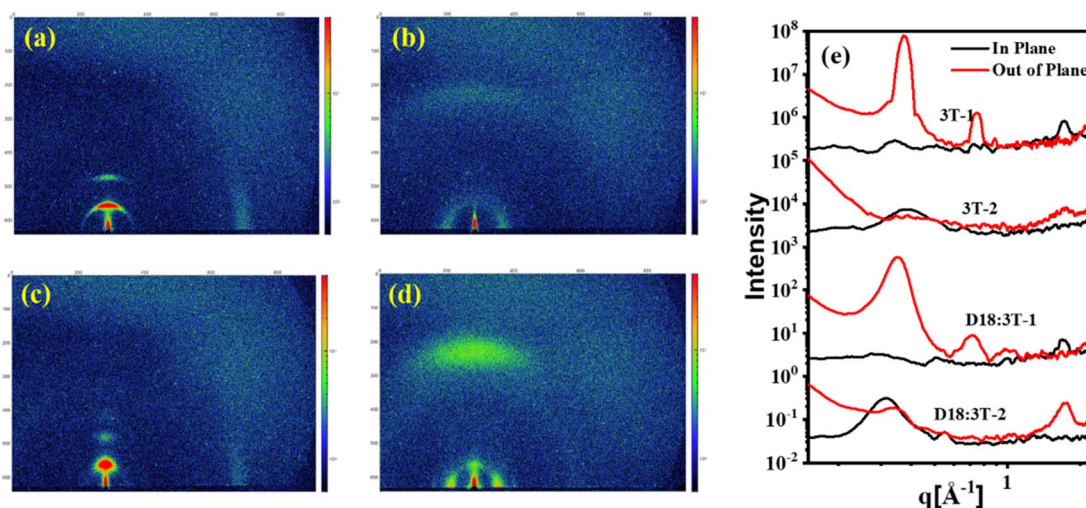

Fig. 4 GIWAXS 2D patterns of (a) the neat **3T-1** film, (b) the neat **3T-2** film, (c) the **D18:3T-1** blend film, and (d) the **D18:3T-2** blend film, and (e) the corresponding 1D line-cuts.
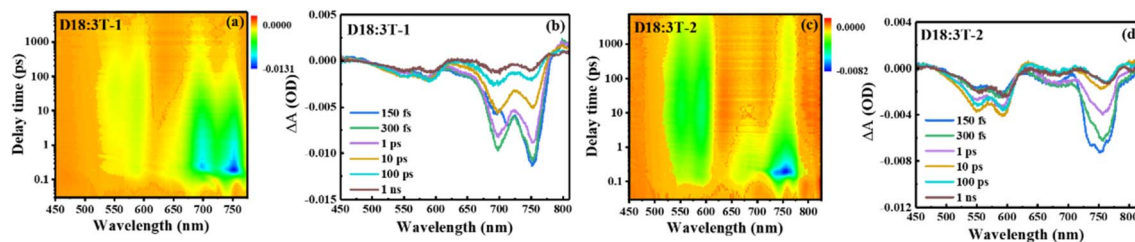
Fig. 5 . (a) and (c) Contour plots of time-resolved absorption difference spectra of the **D18**:**3T-1** and **D18**:**3T-2** blend film; (b) and (d) TA spectra of the **D18**:**3T-1** and **D18**:**3T-2** blend film recorded at selected decay times.

film, demonstrating that poor miscibility and large phase separation exists in the active layer, which agrees well with the morphology study (*vide supra*). The **D18**:**3T-2** blend film mainly adopted face-on orientations with an obvious (010) diffraction peak in the OOP direction, which is beneficial for improving the vertical charge transport. Additionally, the **D18**:**3T-1** blend film shows a larger CCL value of 92.81 Å for the (100) diffraction in the OOP direction. In comparison, a markedly reduced CCL value of 69.26 Å for the **D18**:**3T-2** blend film can be observed. The GIWAXS test results are consistent with AFM measurement. All the observations indicate that a branched side chain can efficiently adjust the molecular orientation and crystallization behavior.

Femtosecond transient absorption spectra

Femtosecond transient absorption (fs-TA) spectra were measured to evaluate the charge transfer dynamic process of the blend films and the results are shown in Fig. 5 and S5.† A pump wavelength of 730 nm is used to selectively excite the acceptors without the donor. For the acceptor films, two ground-state bleaching (GSB) bands mainly appear at about 750 and 697 nm for **3T-1**, and a wide GSB band mainly appears at about 750 for **3T-2**. In comparison with the neat acceptors, a slowly increasing negative signal can be significantly observed with a time delay covering the range of 500–630 nm for the **D18**:**3T-2** blend film, matching well with the absorption features of **D18**, which indicates that an efficient hole transfer process exists at the interface of the donor and acceptor. Subsequently, the recovery signals of blend films at 592 nm are fitted with a double exponential function, and the results are shown in the ESI.† The fast signal represents the recombination of donor excitons, and the slow signal can be considered as the recovery of charge separation excitons. The **D18**:**3T-2** blend film possesses the longest charge separated state lifetime, which can achieve efficient charge transport and photovoltaic performance for OSCs.[43]

Conclusion

In summary, we have designed and synthesized two terthiophene based fully non-fused acceptors **3T-1** and **3T-2** bearing octyl and 2-ethylhexyl side chains for application in highly efficient OSCs. The two acceptors both possess a simple molecular structure and low cost compared with fused ring electron acceptors. Octyl substituted **3T-1** possesses strong crystallinity and poor miscibility, and its blend film with **D18** exhibits an apparent phase separation morphology, leading to an inferior PCE of 2.43%. As for 2-ethylhexyl substituted **3T-2**, it exhibits good solubility and forms an appropriate morphology with a face-on molecular orientation, which results in high and balanced charge mobility in the blend film. Finally, a markedly improved PCE of 11.12% can be achieved processed by non-halogenated *o*-xylene as the solvent, which is the highest value based on terthiophene based non-fused acceptors for OSCs. In all, our research can pave an effective way to design fully non-fused ring acceptors for high performance OSC application.

Conflicts of interest

There are no conflicts to declare.

References

1 P. Cheng, G. Li, X. Zhan and Y. Yang, *Nat. Photonics*, 2018, **12**, 131–142.

2 J. Hou, O. Inganas, R. H. Friend and F. Gao, *Nat. Mater.*, 2018, **17**, 119–128.

3 P. K. Nayak, S. Mahesh, H. J. Snaith and D. Cahen, *Nat. Rev. Mater.*, 2019, **4**, 269–285.

4 Y. Liu, B. Liu, C.-Q. Ma, F. Huang, G. Feng, H. Chen, J. Hou, L. Yan, Q. Wei, Q. Luo, Q. Bao, W. Ma, W. Liu, W. Li, X. Wan, X. Hu, Y. Han, Y. Li, Y. Zhou, Y. Zou, Y. Chen, Y. Liu, L. Meng, Y. Li, Y. Chen, Z. Tang, Z. Hu, Z.-G. Zhang and Z. Bo, *Sci. China: Chem.*, 2022, **65**, 1457–1497.

5 C. Yan, S. Barlow, Z. Wang, H. Yan, A. K. Y. Jen, S. R. Marder and X. Zhan, *Nat. Rev. Mater.*, 2018, **3**, 18003.

This journal is © The Royal Society of Chemistry 2023

J. Mater. Chem. A, 2023, **11**, 7498–7504 | **7503**

6 G. Zhang, J. Zhao, P. C. Y. Chow, K. Jiang, J. Zhang, Z. Zhu, J. Zhang, F. Huang and H. Yan, *Chem. Rev.*, 2018, **118**, 3447–3507.

7 Y. Liu, B. Liu, C.-Q. Ma, F. Huang, G. Feng, H. Chen, J. Hou, L. Yan, Q. Wei, Q. Luo, Q. Bao, W. Ma, W. Liu, W. Li, X. Wan, X. Hu, Y. Han, Y. Li, Y. Zhou, Y. Zou, Y. Chen, Y. Li, Y. Chen, Z. Tang, Z. Hu, Z.-G. Zhang and Z. Bo, *Sci. China: Chem.*, 2021, **65**, 224–268.

8 Q. Yue, W. Liu and X. Zhu, *J. Am. Chem. Soc.*, 2020, **142**, 11613–11628.

9 J. Song and Z. Bo, *Chin. Chem. Lett.*, 2023, 108163.

10 Y. Lin, J. Wang, Z. G. Zhang, H. Bai, Y. Li, D. Zhu and X. Zhan, *Adv. Mater.*, 2015, **27**, 1170–1174.

11 J. Yuan, Y. Zhang, L. Zhou, G. Zhang, H.-L. Yip, T.-K. Lau, X. Lu, C. Zhu, H. Peng, P. A. Johnson, M. Leclerc, Y. Cao, J. Ulanski, Y. Li and Y. Zou, *Joule*, 2019, **3**, 1140–1151.

12 S. Li, C.-Z. Li, M. Shi and H. Chen, *ACS Energy Lett.*, 2020, **5**, 1554–1567.

13 M. Li, Y. Zhou, J. Zhang, J. Song and Z. Bo, *J. Mater. Chem. A*, 2019, **7**, 8889–8896.

14 P. Bi, S. Zhang, Z. Chen, Y. Xu, Y. Cui, T. Zhang, J. Ren, J. Qin, L. Hong, X. Hao and J. Hou, *Joule*, 2021, **5**, 2408–2419.

15 Y. Cui, Y. Xu, H. Yao, P. Bi, L. Hong, J. Zhang, Y. Zu, T. Zhang, J. Qin, J. Ren, Z. Chen, C. He, X. Hao, Z. Wei and J. Hou, *Adv. Mater.*, 2021, **33**, 2102420.

16 M. Deng, X. Xu, Y. Duan, L. Yu, R. Li and Q. Peng, *Adv. Mater.*, 2023, 2210760.

17 X. Zhang, L. Qin, J. Yu, Y. Li, Y. Wei, X. Liu, X. Lu, F. Gao and H. Huang, *Angew. Chem., Int. Ed.*, 2021, **60**, 12475–12481.

18 M. Li, S. Feng, S. Shen, H. Huang, W. Xue, N. Yu, Y. Zhou, W. Ma, J. Song, Z. Tang and Z. Bo, *Chem. Eng. J.*, 2022, **438**, 135384.

19 H. Huang, Q. Guo, S. Feng, C. Zhang, Z. Bi, W. Xue, J. Yang, J. Song, C. Li, X. Xu, Z. Tang, W. Ma and Z. Bo, *Nat. Commun.*, 2019, **10**, 3038.

20 X. Wang, H. Lu, Y. Liu, A. Zhang, N. Yu, H. Wang, S. Li, Y. Zhou, X. Xu, Z. Tang and Z. Bo, *Adv. Energy Mater.*, 2021, **11**, 2102591.

21 X. Zheng, W. Liu, H. Wang, X. Man, G. Ran, X. Yu, H. Lu, Z. Bi, Y. Liu, A. Zhang, W. Ma, X. Xu, Z. Tang, W. Zhang and Z. Bo, *Cell Rep. Phys. Sci.*, 2022, **3**, 101169.

22 Y. N. Chen, M. Li, Y. Wang, J. Wang, M. Zhang, Y. Zhou, J. Yang, Y. Liu, F. Liu, Z. Tang, Q. Bao and Z. Bo, *Angew. Chem., Int. Ed.*, 2020, **59**, 22714–22720.

23 Z. P. Yu, Z. X. Liu, F. X. Chen, R. Qin, T. K. Lau, J. L. Yin, X. Kong, X. Lu, M. Shi, C. Z. Li and H. Chen, *Nat. Commun.*, 2019, **10**, 2152.

24 Z. Yao, Y. Li, S. Li, J. Xiang, X. Xia, X. Lu, M. Shi and H. Chen, *ACS Appl. Energy Mater.*, 2020, **4**, 819–827.

25 X. Ding, X. Chen, Y. Xu, Z. Ni, T. He, H. Qiu, C.-Z. Li and Q. Zhang, *Chem. Eng. J.*, 2022, **429**, 132298.

26 X. Zheng, W. Liu, H. Lu, N. Yu, Y. Wang, H. Huang, S. Li, X. Wang, H. Wang, Y. Liu, X. Xu, Z. Tang and Z. Bo, *Chem. Eng. J.*, 2022, **444**, 136472.

27 J. Gao, X. Zhu, H. Bao, J. Feng, X. Gao, Z. Liu and Z. Ge, *Chin. Chem. Lett.*, 2022, 107968.

28 M. E. Cinar and T. Ozturk, *Chem. Rev.*, 2015, **115**, 3036–3140.

29 T. P. Kaloni, P. K. Giesbrecht, G. Schreckenbach and M. S. Freund, *Chem. Mater.*, 2017, **29**, 10248–10283.

30 B. Kan, M. Li, Q. Zhang, F. Liu, X. Wan, Y. Wang, W. Ni, G. Long, X. Yang, H. Feng, Y. Zuo, M. Zhang, F. Huang, Y. Cao, T. P. Russell and Y. Chen, *J. Am. Chem. Soc.*, 2015, **137**, 3886–3893.

31 B. Kan, Q. Zhang, M. Li, X. Wan, W. Ni, G. Long, Y. Wang, X. Yang, H. Feng and Y. Chen, *J. Am. Chem. Soc.*, 2014, **136**, 15529–15532.

32 J. Zhou, X. Wan, Y. Liu, Y. Zuo, Z. Li, G. He, G. Long, W. Ni, C. Li, X. Su and Y. Chen, *J. Am. Chem. Soc.*, 2012, **134**, 16345–16351.

33 T. Lee, Y. Eom, C. E. Song, I. H. Jung, D. Kim, S. K. Lee, W. S. Shin and E. Lim, *Adv. Energy Mater.*, 2019, **9**, 1804021.

34 J. Zhu, C. Yang, L. Ma, T. Zhang, S. Li, S. Zhang, H. Fan and J. Hou, *Org. Electron.*, 2022, **105**, 106512.

35 Y. Zhou, M. Li, H. Lu, H. Jin, X. Wang, Y. Zhang, S. Shen, Z. Ma, J. Song and Z. Bo, *Adv. Funct. Mater.*, 2021, **31**, 2101742.

36 L. Ma, S. Zhang, J. Ren, G. Wang, J. Li, Z. Chen, H. Yao and J. Hou, *Angew. Chem., Int. Ed.*, 2022, 2214088.

37 H. Lu, X. Wang, S. Li, D. Li, N. Yu, Z. Tang, Y. Liu, X. Xu and Z. Bo, *Chem. Eng. J.*, 2022, **435**, 134987.

38 C. Yang, L. Ma, Y. Xu, J. Ren, J. Hou and S. Zhang, *Sci. China: Chem.*, 2022, **65**, 2604–2612.

39 L. Ma, S. Zhang, J. Zhu, J. Wang, J. Ren, J. Zhang and J. Hou, *Nat. Commun.*, 2021, **12**, 5093.

40 S. Ko, E. Verploegen, S. Hong, R. Mondal, E. T. Hoke, M. F. Toney, M. D. McGehee and Z. Bao, *J. Am. Chem. Soc.*, 2011, **133**, 16722–16725.

41 Y. Wang, T. Hasegawa, H. Matsumoto, T. Mori and T. Michinobu, *Adv. Funct. Mater.*, 2017, **27**, 1604608.

42 Q. Liu, Y. Jiang, K. Jin, J. Qin, J. Xu, W. Li, J. Xiong, J. Liu, Z. Xiao, K. Sun, S. Yang, X. Zhang and L. Ding, *Sci. Bull.*, 2020, **65**, 272–275.

43 Y. Dong, H. Cha, H. L. Bristow, J. Lee, A. Kumar, P. S. Tuladhar, I. McCulloch, A. A. Bakulin and J. R. Durrant, *J. Am. Chem. Soc.*, 2021, **143**, 7599–7603.

7504 | *J. Mater. Chem. A*, 2023, **11**, 7498–7504

This journal is © The Royal Society of Chemistry 2023